Nanoscale

Accepted Manuscript

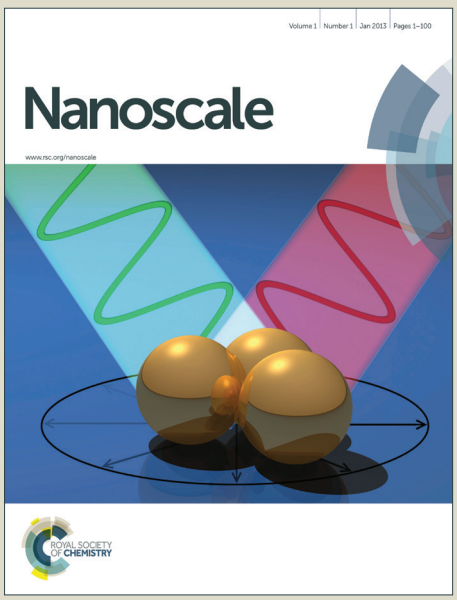

ROYAL SOCIETY OF CHEMISTRY

www.rsc.org/nanoscale

Nanoscale

RSCPublishing

ARTICLE

Bifunctional Au@Pt core-shell nanostructures for *in-situ* monitoring of catalytic reactions by surface-enhanced Raman scattering spectroscopy

Cite this: DOI: 10.1039/xoxxoooooox

Received:
Accepted:

DOI: 10.1039/xoxxoooooox

www.rsc.org/nanoscale

Zhi Yong Bao,[‡a] Dang Yuan Lei,[‡*a,b] Ruibin Jiang,[c] Xin Liu,[a,d] Jiyan Dai,[a,b] Jianfang Wang,[c] Helen L. W. Chan,[a] Yuen Hong Tsang*[a]

Optical probes of heterogeneous catalytic reactions are of great importance for in-situ determination of the catalytic activity and monitoring of the reaction process. Surface-enhanced Raman scattering (SERS) spectroscopy could be used as a sensitive optical probe for this purpose provided that plasmonic metal nanoparticles for Raman enhancement are properly integrated with catalytic metals to form a single entity. Herein we present a facile approach for synthesizing Au@Pt core/shell nanostructures with controllable surface density of sub-5 nm Pt nanoparticles on the surface of Au nanorods. Systematic investigations on both SERS and catalytic activities of the hybrid nanostructures reveal an optimized surface coverage of Pt. More importantly, we demonstrate that, due to their dual functionalities, the hybrid nanostructures are able to track the Pt-catalysed reaction in real time by measuring the SERS signals of the reactant, intermediate and final products. This SERS-based synergy technique provides a novel approach for quantitatively studying catalytic chemical reaction processes and is suitable for many applications such as reduction and oxidation reactions in fuel cells and catalytic water splitting.

Introduction

Noble metal nanoparticles(NPs)made of, for example, Au and Ag have attracted extensive research attention due to their distinctive plasmonic behaviours, which have been employed in a wide range of local near-field related applications, including fluorescence enhancement,[1,2] surface-enhanced Raman scattering (SERS),[3-5] photothermal therapy,[6,7] and more recently in catalysis, photocatalysis and photovoltaics.[8-11] Integration of plasmonic NPs with catalytically-active metals such as Pt and Pd has been obtained to achieve both SERS and catalytic functionalities in a single entity. The resultant bifunctional, hybrid nanostructures have been used to characterize different types of Pt- or Pd-catalyzed reactions by monitoring the SERS response.[12-21] Early demonstrations include the use of Au or Ag NPs coated with a complete shell of Pt or Pd,[13-17] and Pd islands deposited on Au nanoshells.[18] More recently, bifunctional Au/Pt/Au nanoraspberries have been synthesized for quantitatively in-situ monitoring of Pt-catalyzed reactions by application of SERS.[19] Characterizing the kinetics of catalytic reactions has also been demonstrated using simultaneously immobilized Au and Pt NPs on a substrate.[20]

Despite of the significant progress made over the last few years, the following design considerations must be addressed when selecting a target nanostructure that exploits plasmonic effects for SERS enhancement and Pt or Pd for catalysis purpose. The first consideration is the optimization of plasmonic near-field enhancement that directly determines the SERS intensity. In general, one important criterion has to be taken into account for maximizing the near-field enhancement in NPs of regular shapes, namely matching the localized surface plasmon resonance with the excitation laser wavelength and across the Stokes frequency range. The bifunctional NPs used previously often have a spherical shape, whose localized surface plasmon resonance is difficult to be tuned flexibly,[15-21] and hence restrict their applications to specific excitation wavelengths. The second design consideration is to have the largest possible surface area of Pt or Pd so as to obtain high catalytic efficiency, which usually requires the use of sub-5 nm catalytic metal NPs and thus a complete shell of Pt or Pd is obviously less favorable.[13,15,16,19] The third one is to control the surface coverage of catalytic NPs on plasmonic metal cores such that a balance between SERS enhancement and catalytic efficiency can be achieved due to the fact that large-area coating of metals on a plasmonic NP significantly degrade its near-field enhancement.[16] This consideration has not been fully taken into account in previous studies.[13-19] Last but not least, in addition to existing approaches using NP films immobilized on a solid support,[17,18,20,21] it is necessary to monitor catalytic reactions directly in colloidal suspension because many chemical reactions take place in solution environment.

It is worthwhile pointing out that the SERS or tip-enhanced Raman scattering (TERS) technique has also been used to monitor a general class of chemical reactions,[22-28] such as the photocatalytic decomposition reaction at the interface between metal or metal oxide NPs and flat metal surfaces,[24,25] and plasmonic "hot" electrons-mediated or plasmon-driven reactions.[28,29]

In this study, a seed-mediated growth approach was employed to fabricate sub-5 nm Pt NPs-decorated Au nanorods (NRs) with tunable localized surface plasmon resonance wavelength. The surface density of Pt NPs is readily controlled by adjusting the molar ratio of the precursor reaction solution and its effects on the SERS enhancement and catalytic efficiency are examined in a systematic manner in order to identify an optimized surface coverage of Pt. Finally, the optimized structure is used to monitor in real time the catalytic reaction process of 4-nitrothiophenol (4-NTP) to 4-aminothiophenol (4-ATP) process by observing the changes in the intensities of characteristic Raman peaks with increased amount of reductant.

Experimental section

Synthesis of starting Au NRs and Au@Pt core/shell nanostructures

The chemicals, tetrachloroauric (III) acid ($HAuCl_4$), cetyltrimethylammonium bromide (CTAB), silver nitrate ($AgNO_3$), hexachloroplatinic (IV) acid (H_2PtCl_6), ascorbic acid (AA), 4-nitrothiophenol, 4-aminothiophenoland sodium borohydride were purchased from Sigma and all chemicals were used without further purification. Ultrapure water was used for all experiments. The starting Au NRs were grown according to previous seed-mediated method.[30] Specifically, the seed solution was prepared by mixing $HAuCl_4$ (0.01 M, 0.25 mL) and CTAB (0.1 M, 9.75 mL) in a 15 mL plastic tube. An ice-cold $NaBH_4$ solution (0.01 M, 0.6 mL) was then injected quickly into the mixture solution, followed by rapid inversion for 1 min. The seed solution was kept at room temperature for at least 2 h before use. To grow Au NRs, $HAuCl_4$ (0.01 M, 2.0 mL) and $AgNO_3$ (0.01 M, 0.4 mL) were mixed with CTAB (0.1 M, 40 mL) in a 50mL plastic tube. HCl (1.0 M, 0.8 mL) was then added to adjust the pH of the solution to 1-2, followed by the addition of AA (0.1 M, 0.32 mL). Finally, the seed solution (10 μL) was injected into the growth solution. The solution was gently mixed for 20 s and left undisturbed at room temperature for at least 6 h before use. Then the Au NRs were centrifuged two times and redispersed in water. With the purpose of tailoring the surface plasmon resonance to match the excitation laser wavelength at 633 nm in SERS measurements, the starting Au NRs were oxidized by adding a certain amount of $HAuCl_4$ (0.01 M) and the longitudinal plasmon wavelength was therefore tailored to around 633 nm. Due to oxidization of the added Au^+, the Au NRs are oxidized anisotropically. The oxidation often takes place at the NR ends more quickly than at the lateral side. Therefore, the aspect ratio of the Au NR becomes smaller and the plasmon resonance wavelength shifts to blue.

The as-prepared Au NRs were precipitated by centrifugation (6300 g, 10 min), washed once with water (10 mL) and then redispersed in water (10 mL). A mixture of CTAB (3 mL, 0.1 M) and AA (0.4 mL, 0.1 M) were added to the resultant solution, followed by adding four different amounts of H_2PtCl_6 (0.01 M) to have different surface coverage of Pt on Au. The four mixed solutions were then placed in an oven set at 60°C overnight. The resultant Au@Pt core/shell nanostructures were separated by centrifugation (6300 g, 10 min) and finally redispersed in water.

Characterization methods

The prepared nanostructures were respectively drop-casted on a TEM grid to perform high-resolution morphology characterizations and EDX element mappings using a JEM2100F TEM system operating at 300 kV. The Raman spectra were recorded in solution using a Raman spectrometer from Princeton Instruments (HORIBA HR800) with excitation laser wavelength at 633 nm. The laser power (with a beam diameter of ~2 μm) was approximately 1 mW and the integration duration was kept at constant of 5 s. The excitation light and the scattering light were focused and collected by the same long-working distance objective (W.D. 3.18 mm, NA 0.7, Mag. 60x). The extinction spectra of the metal NRs were obtained on a UV-Vis absorption spectrometer (Shimadzu Scientific Instruments, UV2550).

Results and discussion

Figure 1A shows the TEM image of the as-prepared Au NRs of ~70 nm in length and ~20 nm in diameter. Fig. 1B and 1C show the low and high-magnification TEM images of Au@Pt core/shell nanohybrids, respectively. Compared to Fig. 1A, one can clearly see from Fig. 1B that all the Au NRs are successfully coated with small Pt NPs. Fig. 1C further reveals that the whole surface of each Au NR is uniformly coated by a large number of well-dispersed, discontinuous Pt NPs with diameters of 2-5 nm, which is confirmed by the high-magnification TEM image taken at one end of the Au NR (see the inset in Fig. 1C). As discussed above, such configuration is particularly important to achieve strong dual functionalities because the sub-5 nm Pt NPs are expected to have robust catalytic activity benefiting from the large surface area to volume ratio while a significantly-enhanced local electromagnetic field can be generated at the uncoated areas of Au NRs due to the creation of nanometer-scale gaps. In addition, the high-magnification TEM image also shows that both the Au NRs and most of Pt NPs are single-crystalline and the measured lattice spacing of 0.226 and 0.235 nm correspond to the (111) planes of Pt and Au, respectively (Details shown in Figure S1). Figure 1D and 1E show the element mapping of Au and Pt in the hybrid nanostructure, respectively, which corroborate that the Au NRs are uniformly wrapped with Pt NPs. The EDX map spectrum of the hybrid structure also suggests successful coating of Pt on Au. Except the peaks of Cu and C coming from the TEM supporting grid, no other peaks have been observed in the EDX spectrum, indicating high purity of the as-prepared samples.

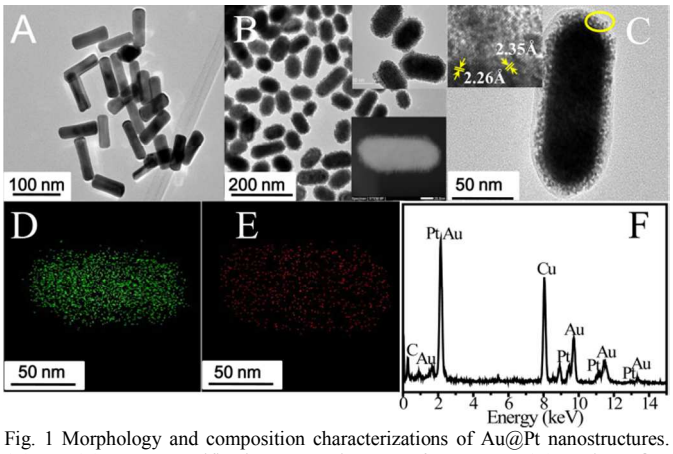

Fig. 1 Morphology and composition characterizations of Au@Pt nanostructures. (A) & (B) Low-magnification TEM images of Au NRs (A) and Au@Pt nanostructures (B). (C) High-magnification TEM image of an Au@Pt nanohybrid with crystal-lattice mapping of the area enclosed by the yellow circle shown in the inset. (D-F) Elemental mapping of Au (D) and Pt (E) in the Au@Pt nanostructure and the corresponding EDX spectrum from Au@Pt nanohybrids (F).

In order to examine systematically the effects of Pt surface coverage on the catalytic activity and SERS response of the hybrid Au@Pt core/shell nanohybrids, four samples were prepared with different molar ratios of the Pt precursor and Au NRs. In this

experiment, the amount of the selected Au NRs was fixed (10 mL, 10 nM) and four different amounts (60 µl, 120 µl, 180 µl and 240 µl) of H_2PtCl_6 (0.01 M) were added separately with details described in the experimental section. For the purpose of convenience, the resulting Au@Pt core-shell nanostructures were labelled as Au@Pt-a, Au@Pt-b, Au@Pt-c and Au@Pt-d, with their TEM images shown in Fig. 2(A-D), respectively. One can clearly see from the images that the gradual increase of the amount of Pt precursor has little effects on the NP size but significantly increases the surface density of Pt NPs, which results in a uniform and dense distribution of catalytically-active spots over the Au NR surface. Their optical properties will be discussed in the following sections.

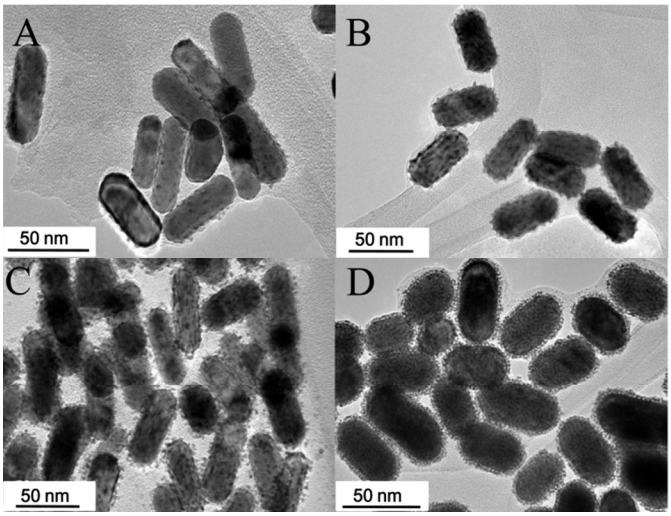

Fig. 2 (A-D) TEM images of the Au@Pt hybrid nanostructures with gradual increase in the surface coverage of Pt NPs on Au NRs. They were labelled as Au@Pt-a, Au@Pt-b, Au@Pt-c, and Au@Pt-d, respectively.

Prior to the growth of Pt NPs, we have carefully tailored the length-to-diameter aspect ratio of Au NRs (~50 nm in length and ~20 nm in diameter) and tuned their localized surface plasmon resonance close to the excitation laser wavelength. Fig. 3A shows the UV-Vis absorption spectra of the as-prepared Au NRs (1), the oxidized Au NRs (2), and the Au@Pt-d sample. As can be seen from the Figure, the starting Au NRs (1) display two absorption peaks at 515 and 693 nm (red curve), corresponding to the transverse and longitudinal localized surface plasmon resonances, respectively. After oxidation by adding additional $HAuCl_4$ (0.01 M) to the original Au NRs solution, the longitudinal resonance wavelength blue-shifts to 628 nm while the transverse resonance wavelength remains unchanged (see the black curve in Fig. 3A). Simultaneously, the colour of the solution changes from light-grey to sky-blue (see the photograph images in Fig. 3A) due to the strong absorption in the red and yellow range of white light by the NRs. Such flexible modulation of localized surface plasmon resonance wavelength makes the Au@Pt core-shell nanohybrids more versatile in matching different excitation wavelengths than the spherical NPs used in previous studies.[15-21] The other advantage associated with this resonance tuning method is that no other chemicals or ions are introduced and therefore the purity of the samples can be ensured. Fig. 3A also shows that further growth of Pt NPs on the Au NRs (2) results in little changes in the two resonance positions of the hybrid structure (i.e. Au@Pt-d) but induces significant damping of the longitudinal surface plasmon resonance amplitude, indicating a decrease in the plasmonic near-field enhancement as we will see from the SERS results later.

Fig. 3B shows the UV-Vis absorption spectra for the four hybrid structures, Au@Pt-a, -b, -c and -d, with Pt surface coverage increasing gradually as shown by the TEM images in Fig. 2. The absorption spectra clearly demonstrate that increasing the surface coverage of Pt on Au significantly damps the longitudinal resonance amplitude, resulting in lower and lower absorption intensity. This could be attributed to the fact that the existence of Pt on the surface Au NRs prevents them from efficient excitation of surface plasmons by light and also provides additional ohmic loss channels to plasmon decay. We also note that after coating of Pt, the transverse resonance at 525 nm exhibits little changes in both the resonance position and amplitude. This can be understood from the fact that the electric near-field distribution profiles for the two plasmon resonances are completely different. For the longitudinal plasmon resonance the electric field is tightly localized within a small area at the two ends of the NR, which implies that a small perturbation such as attachment of Pt particles to the NR ends could result in enormous changes to the resonance properties; for the transverse plasmon resonance, the electric field with much weaker intensity is widely distributed over the whole transversal surface and thus much insensitive to changes in the local environment. Note that the Pt particles themselves have no observable absorption characteristic peak in the visible range. The corresponding photographs shown in the inset of Fig. 3B demonstrate a gradual color change from blue-brown (Au@Pt-a) to blue-black (Au@Pt-d) with the increase of Pt particles attached on the Au surfaces.

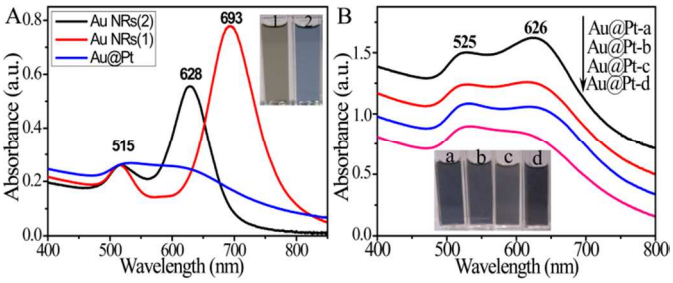

Fig. 3 (A) Absorption spectra of Au NRs with two different aspect ratios (black and red curves) and Au@Pt-d core-shell nanostructures (blue curve). Insets are the photographs of the two Au NR samples. (B) Absorption spectra were measured for the four hybrid nanostructures, Au@Pt-a, -b, -c and -d samples shown in Fig. 2. Insets are their corresponding photographs.

To explore the catalytic property of the Au@Pt core/shell nanostructures, the 4-NTP molecule was chosen as analyte in the experiments. A quartz vessel (4 mL capacity) was used as the catalysis reactor in which each of the following five samples, including Au NRs, Au@Pt-a, -b, -c and -d hybrid nanostructures, was mixed separately with the 4-NTP solution. The catalytic activity of each structure was then determined by recording the absorption intensity of 4-NTP at wavelength 410 nm, which is due to the formation of 4-nitrophenolate ions from 4-NTP in the alkaline condition caused by the addition of $NaBH_4$. The detailed catalytic mechanism can be seen from Scheme 1: The Pt NPs act as a catalyst and the catalytic reaction takes place at their surfaces. The borohydride ions react with Pt, forming a metal hydride to catalyse 4-NTP molecules.[31,32] We recorded the absorption intensity as a function of reaction time and calculated the catalytic reaction rate using the well-established pseudo-first-order approximation.

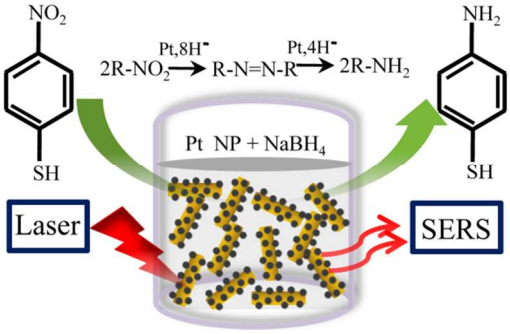

Scheme 1 Representation of the reduction of 4-NTP by $NaBH_4$ to 4-ATP, which takes place on Au@Pt superstructure surfaces. The reaction is catalyzed by the Pt NPs, while the SERS signal is brought about by local optical fields of the Au NRs.

Figure 4A-C renders time-dependent UV-Vis absorption spectra of the 4-NTP solution (10^{-3} M) mixed respectively with the Au@Pt-b, Au@Pt-c and Au@Pt-d nanostructures. It can be clearly seen that the absorption intensity of 4-NTP at wavelength 410 nm decreases with increasing $NaBH_4$ in the presence of the Au@Pt hybrid nanostructures and that the decreasing rate accelerates with the surface coverage of Pt NPs. In this way, as soon as we added the $NaBH_4$, these Pt NPs started the catalytic reduction by relaying electrons from the donor BH_4^- to the acceptor 4-nitrophenol right after the adsorption of both onto the particle surfaces. In addition, the addition of a small amount of Au@Pt NPs can cause fading and ultimate bleaching of the yellow colour of the reaction mixture. Figure 4D shows the normalized concentration of 4-NTP, which is extracted from the absorption intensity and plotted as a function of reaction time in each of the five structures used in this study. By fitting each curve with an exponential decay function under the pseudo-first-order approximation, an apparent rate constant for the degradation of 4-NTP in each catalyst can be extracted to compare quantitatively the catalytic performance. Though the inter-band transitions of Au and Pt nanoparticles at 410 nm contribute to the total extinction of the reactant, their contribution is constant and causes no changes in the measured extinction.[33]

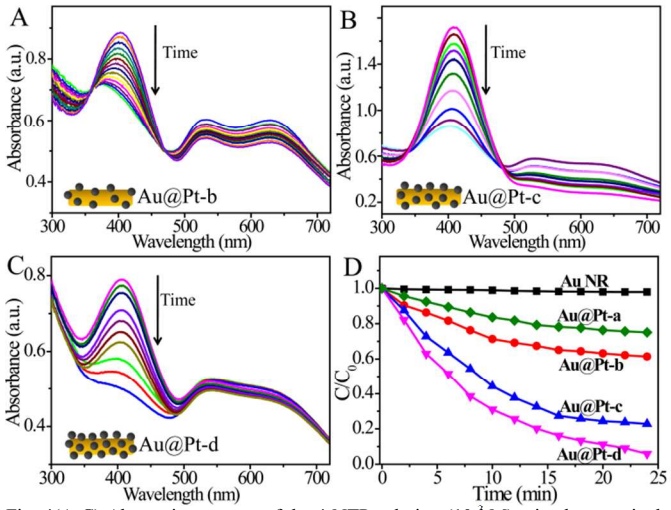

Fig. 4(A-C) Absorption spectra of the 4-NTP solution (10^{-3} M) mixed respectively with the Au@Pt-b, Au@Pt-c and Au@Pt-d superstructures as a function of increasing the amount of $NaBH_4$. The original $NaBH_4$ solution has a concentration of 5 mM and we added it to the reactant stepwise while measuring the absorption spectrum of the whole reactant. This means that the effective concentration of $NaBH_4$ in the reactant solution increases from 3.33 x 10^{-5} M to 3.13 x 10^{-4} M between the top and bottom spectra in the plot. (D) Normalized concentration of 4-NTP, extracted from the corresponding absorption intensity as a function of reaction time in the presence of the four Au@Pt nanostructures and the bare Au NRs.

For direct comparison of catalytic efficiency between different Au@Pt nanohybrids, $\ln(A_{410(t)}/A_{410(0)})$ as a function of reaction time, in which $A_{410(t)}$ and $A_{410(0)}$ are the absorbance at successive intervals and the initial stage, respectively, are depicted in Figure 5A. A linear relationship is obtained for all the nanohybrids samples, indicating a pseudo-first-order kinetics in the reduction reaction. The reaction rate constants k are found to be 1.8, 2.7, 5.2, and 6.3×10^{-4} s^{-1} for Au@Pt-a, b, c and d, respectively, as calculated from the linear fit equation $\ln(A_{410(t)}/A_{410(0)}) = -kt$. However, it is difficult to calculate the exact mole percentage of 4-ATP because the original mole percentage of the self-assembled monolayer 4-NTP cannot be measured. In sharp contrast, the concentration of 4-NTP remains unchanged in the presence of the bare Au NRs, demonstrating that Au NRs have none or very weak catalytic activity. This is due to the fact that in the absence of a proper catalyst, the thermodynamically favourable reduction of 4-NTP is not launched and thus the peak at 410 nm remains unaltered even after a couple of days as reported in the literature.[16]

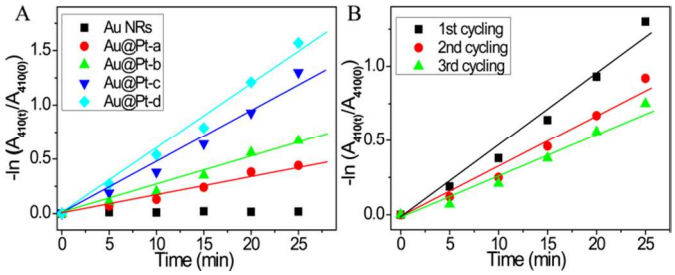

Fig. 5 (A) Plots of $\ln(A_{410(t)}/A_{410(0)})$ as a function of reaction time for the reactions catalyzed by Au NRs, Au@Pt-a, b, c, and d nanohybrids samples, respectively. (B) Three cycles of catalytic activity of the Au@Pt-c hybrids in decomposing 4-NTP. The solid lines are linear fits to the measured data points (symbols).

The recyclability of catalysts is an important issue in practical applications. To evaluate the feasibility of the recyclable property for the Au@Pt core/shell nanostructures, three successive cycles of catalytic reactions using the same Au@Pt-c nanohybrids were carried out as shown in Figure 5B. After each cycle, the nanohybrids were centrifuged by DI water and then air-dried. Though there is a slight change in the reaction rate constant after three cycles, the k value still remains close to that of the original Au@Pt hybrids. The main reason for the decrease in the catalytic efficiency may be due to the loss of the catalysts during the recycling process. The results demonstrate that these nanohybrids have good catalytic stability in aqueous solution. Besides, we investigated the morphologies of the Au@Pt hybrids before and after the catalytic reaction because the dual functionalities of SERS enhancement and catalytic property in the Au@Pt nanohybrids are based on the hybrid nanostructures containing plasmonic metal cores and catalytic metal shells. From Figure S1 it is found that, even after three cycles, the morphologies of the coated Pt nanoparticles as well as the Au NRs keep almost unchanged and each Au NR is uniformly coated by a large number of well-dispersed Pt NPs with diameters of 2-5 nm. In addition, we find no colloidal aggregations or changes in their shapes. Such morphology preservation might be due mainly to the low laser power and good heat dissipation of the liquid solution surrounding the Au@Pt nanohybrids. All these results confirmed that these Au@Pt core/shell nanostructures can be recycled.

Once we have determined the catalytic activity of the hybrid structures, in the following we move to study their SERS sensitivities, one of the dual functionalities. In this experiment, we mixed the solution of 4-NTP and each of the metal nanostructures,

and kept the mixture for a certain period of time to allow for a self-assembled monolayer of 4-NTP adsorbed on the surface of metal nanostructures. Fig. 6A shows the SERS spectra of 4-NTP collected from the Au NRs and Au@Pt core/shell nanostructures. The Raman band at ca.1078, 1345 and 1572 cm^{-1} can be assigned respectively to the S-C stretching vibration, symmetric nitro stretching vibration and phenyl ring modes, respectively. To compare quantitatively the SERS enhancements from the five structures, Fig. 6B shows direct comparison between the measured Raman intensities at the four characteristic Raman peaks of 4-NTP for the five samples, which clearly demonstrates that the Raman intensity of 4-NTP decreases significantly with the increase of Pt coverage.

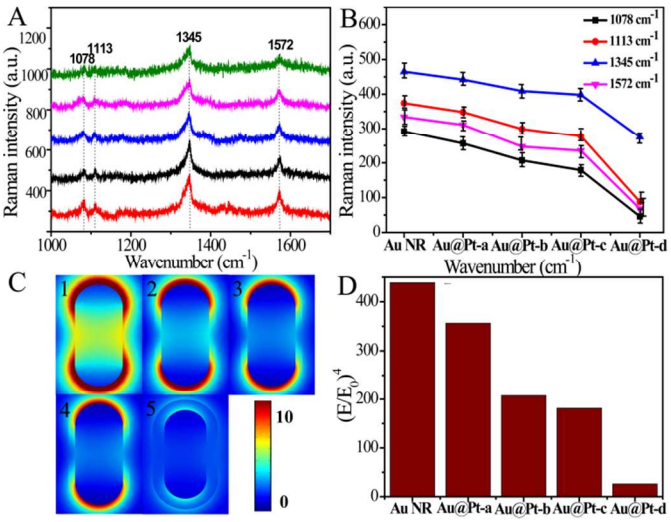

Fig. 6 Measured SERS responses and calculated near-field enhancement factors. (A) SERS spectra collected from 4-NTP (10^{-3} M) self-assembled on the surface of Au and Au@Pt nanohybrids. (B) Raman intensities at bands 1078 (black square), 1113 (red circle), 1345 (blue up-triangle) and 1572 cm^{-1} (purple down-triangle) extracted from (A), with each data point representing an average value from three measurements. The solid lines are guide to the eyes. (C) Cross-sectional view of the normalized electric-field intensity distribution profiles for the bare Au NR (1) and Au@Pt nanohybrids (2-5 for Au@Pt-a,-b, -c and -d).The shell thickness of the effective medium is 3 nm for Au@Pt-a, -b, and -c and 6 nm for Au@Pt-d as determined from the TEM images shown in Fig. 2. (D) Spatially-averaged biquadratic field enhancement factors for Au and Au@Pt nanohybrids by integrating the enhancement over a closed surface at a distance of 1 nm from the NP surface. In this study, all the Raman band intensities were directly extracted from the spectra by measuring their peak heights.

To understand the underlying mechanism responsible for the different SERS enhancements observed as well as how the plasmonic behaviour in the Au NR is governed by the dielectric variation in the shell, we employed the finite-element method, implemented in the multi-physics COMSOL software, to calculate the electric near-field enhancement factors for the four hybrid structures and the bare Au NR excited at wavelength 633 nm with incident polarization along the long axis of the rod. Here the dielectric response of the shell on the Au NR (50 nm in length and 22 nm in diameter) is modelled as an effective medium consisting of air and Pt NPs (3 nm in diameter) with the volume fraction of Pt determined from the TEM images shown in Fig. 2 (3.84%, 4.97%, 5.37%, and 13.93% for Au@Pt-a, -b, -c and -d, respectively). Fig. 6C presents the field intensity distribution profiles for the Au NR and Au@Pt nanohybrids, which show that the field intensity is suppressed gradually with increasing volume fraction of Pt (from Fig. 6C1 to 6C5). Since the 4-NTP molecules are expected to adsorb over the whole surface of metal NPs, the measured Raman intensity should be proportional to the integration of the biquadratic E-field enhancement over the NP surface.[34,35]

$$I_{SERS} = \frac{1}{\Omega}\int \left(\frac{E}{E_0}\right)^4 dS$$

Where Ω is the area of a closed surface enclosing the nanostructure with 1 nm distance from the NP surface and S is the surface integration element. Fig. 6D illustrates the spatially-averaged E-field enhancement factors calculated with the above equation for the five structures, showing perfect agreement with the SERS results. This confirms that the degraded SERS response in Au@Pt nanohybrids indeed comes from the field-shielding effect caused by the Pt coating and that larger surface coverage of Pt (corresponding to stronger catalytic activity) results in smaller near-field enhancement.

It should be noted that the SERS signals are not strong. It may be due to following two reasons: (1) In the SERS experiment, we mixed the solution of 4-NTP and each of the metal nanostructures, and to allow for a self-assembled monolayer of 4-NTP adsorbed on the surface of metal nanostructures, then washed out the residual 4-NTP molecules and diluted the mixed solution. Therefore, it is assumed that the efficient 4-NTP molecules contributing to SERS signal enhancements are relatively low; (2) the residual CTAB molecules on the surface of the Au@Pt core/shell nanostructures could cause poor affinity between the hybrid nanostructures and the adsorbed molecules, which also results in a weak SERS intensity.

The nanoparticle concentration will have without question an important impact on the SERS intensity. In order to optimize the SERS signal, a series of particle concentrations have been chosen in the SERS measurements to determine the maximized enhancement. For example, the SERS signal collected for the metal NPs with concentration of 10^{-11}-10^{-12} M would be extraordinarily low compared to a higher value like 10^{-9}-10^{-10} M (concentrations determined according to the Beer-Lambert Law, details not shown here). But slight variations in particle concentration would not have a significant impact on the relative SERS intensity.

To verify whether tuning of the NR surface plasmon resonance prior to Pt coating actually contributes to the improvement in the SERS intensity or not, additional control experiments have been carried out. On the one hand, two types of Au NRs with different surface plasmon resonance wavelengths were chose to perform the SERS measurements in an identical condition (Au NP concentration, analyte concentration and laser power, etc.). The collected SERS results were shown in Figure S2A, from which it is clearly seen that the SERS signal can be significantly improved by tailoring the surface plasmon resonance wavelength of Au NRs (628 nm, black curve) close to the laser excitation wavelength (633 nm). The data were collected randomly from several points and the averaged spectra were shown here. On the other hand, we carried out the same SERS measurements for the two types of Au nanorods by changing the laser excitation wavelength to 488 nm, with results shown in Figure S2B. One can clearly see that the Raman intensity is significantly decreased due to the mismatch between the NR plasmon resonance wavelength and the laser wavelength. Because the Au@Pt core/shell nanostructures have a good reproducibility across the entire substrate, it is believed that tuning of the rod SPR prior to Pt coating actually contributes to the improvement in the SERS intensity.

In addition to the requirements of recyclability and stability for an ideal SERS substrate, reproducibility of the SERS measurements with the substrate must be validated. The relative standard deviation (RSD) of major Raman peaks is often used to estimate the reproducibility of SERS signals. Figure 7 shows the Raman spectra of the 4-NTP molecules adsorbed on the Au@Pt-c sample, randomly collected from a number of locations on the substrate. Using these

Raman spectra one can calculate the RSD spectrum. The maximal RSD value of the signal intensities for the major SERS peaks is observed to be below 0.2, indicating that the Au@Pt-c core/shell nanostructures have a good reproducibility in SERS measurements. From Figure 7 it can also be found that, although the SERS signals are not very strong, the reproducibility and stability of the substrate are fairly good.

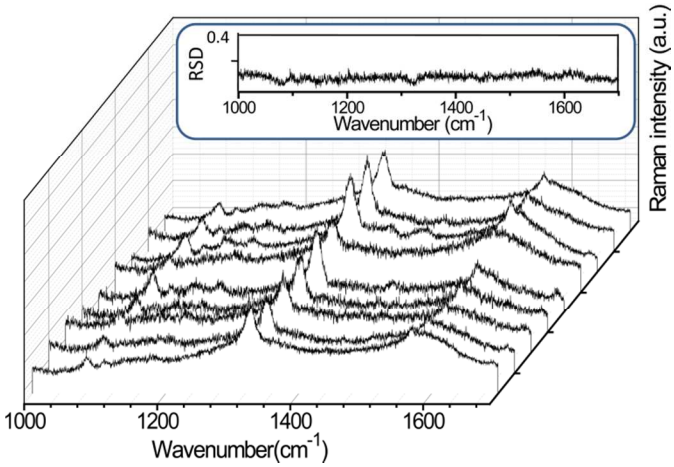

Fig. 7 SERS and RSD spectra of the 4-NTP molecules in the spectral range of 1000 - 1700 cm^{-1}, randomly collected from a number of locations on the Au@Pt-c substrate.

It is well known that sub-5 nm Pt NPs own an excellent catalytic property due to their favourable electronic characteristics and huge surface area to volume ratio, and these small NPs usually have a poor SERS response. However, the hybrid structure can afford a platform for these Pt NPs to benefit from the field enhancement effect of the Au NR, which is the basis for realizing the bifunctional property and allows us to in-situ monitor the catalytic reaction process by recording the SERS response in real time. In the experiment, the Au@Pt-c structure was chosen as the optical probe because it exhibits a good balance between the catalytic activity and the SERS enhancement. The SERS spectrum was recorded each time after adding the $NaBH_4$ aqueous solution of 5 μL (10^{-3} M) to the Au@Pt solution of 600 μL (0.2 nM) with self-assembled 4-NTP on the NP surface. The aqueous solution of $NaBH_4$ was continuously added till all the 4-ATP molecules were decomposed completely.

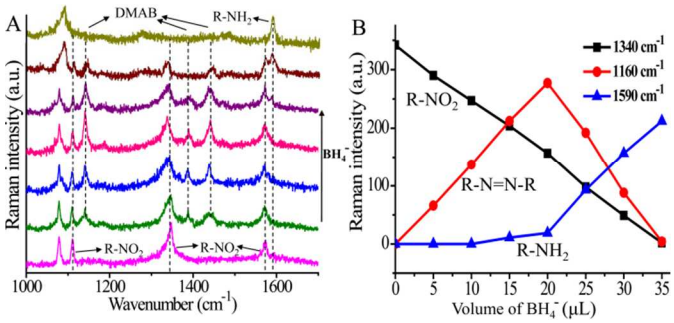

Fig. 8 SERS spectroscopy recorded upon addition of different amounts of the reducing reagent $NaBH_4$ in catalysing 4-NTP to 4-ATP with Au@Pt-c nanohybrids. (A) Raman spectra recorded from 4-NTP molecules adsorbed on the surfaces of the Au@Pt-c nanohybrids each time after addition of the $NaBH_4$ solution of 5 μL (10^{-3} M). (B) Raman intensities extracted from (A) at the bands 1340, 1160 and 1590 cm^{-1}, corresponding to the groups of $R\text{-}NO_2$, R-N=N-R and $R\text{-}NH_2$, respectively, and reflecting the relative concentrations of 4-NTP, 4,4′-DMAB and 4-ATP as a function of $NaBH_4$ added to the reaction.

Figure 8A shows a series of Raman spectra collected from the mixed solution in sequence of the addition of $NaBH_4$ (from bottom to top). The Raman spectrum at the bottom demonstrates that the reactant is pure 4-NTP as the three characteristic peaks at 1113, 1345 and 1572 cm^{-1} are clearly observed. Upon addition of the solution of $NaBH_4$, the intensities of the Raman peaks associated with 4-NTP start to decrease immediately and three new peaks at 1140, 1385 and 1434 cm^{-1} appear accordingly, which can be assigned to the vibrational modes of 4,4'-dimercapto-azobenzene(4,4′-DMAB), an intermediate product. Specifically, these three new Raman peaks correspond to the C-N symmetric stretching, N=N stretching, and C-H in-plane bending modes in 4,4′-DMAB, respectively.[23] More interestingly, the intensities of the Raman peaks for 4,4′-DMAB significantly increase with further addition of $NaBH_4$ (from the green to red spectra) and then abruptly decrease till nearly zero (from the black to dark-yellow curve), further corroborating its character as an intermediate product. Meanwhile, the intensities of the peaks for 4-NTP also fade and vanish till zero and a new peak at 1590 cm^{-1},which corresponds to the amino vibrational mode, emerges accordingly and finally dominates the spectrum. We summarize the observations made above in Fig. 8B by plotting the Raman intensities of three characteristic peaks with each associated with the reactant –4-NTP, the intermediate product –4,4′-DMAB and the final product –4-ATP. More importantly, it provides quantitative information about their relative concentrations in the reaction process. It is also important to note that the 4,4′-DMAB increases while the 4-NTP decreases with adding $NaBH_4$. After addition of a certain volume of $NaBH_4$ (20 μL in our case), the amount of 4,4′-DMAB decreases while the amount of 4-ATP arises rapidly since this conversion reflects a sequential hydride reduction of 4-NTP to 4,4′-DMAB and finally to 4-ATP. After adding a sufficient volume of BH_4^- (35 μL in our case), the 4-NTP and 4,4′-DMAB both transform completely and the product is 4-ATP only.

Conclusions

In conclusion, we have prepared Au@Pt core/shell nanostructures using a facile wet chemical method and the hybrid structures synthesized exhibit tunable localized surface plasmon resonance, excellent catalytic activity and strong SERS enhancement. We have demonstrated that the dual functionalities, catalysis and SERS, of the hybrid structures can be readily tailored by adjusting the surface decoration density of Pt NPs on the surfaces of Au NRs and a balance between them can be achieved at an optimal surface density. The optimized hybrid nanostructure has been used as a sensitive optical probe to in-situ monitor the catalytic reaction process by recording the SERS response in real time, enabling the determination of the intermediate and final products and their quantities. We believe that this SERS-based synergy technique could be applied to a more general class of chemical reactions and study the reaction process both qualitatively and quantitatively by recording both the Raman peak positions and intensities.

Acknowledgements

The authors acknowledge the financial support by the Hong Kong Research Grants Council (ECS Grant No. 509513 and GRF Grant No. 526511), the Natural Science Foundation of China (Grant No. 11304261) and the Hong Kong Polytechnic University (Grant Nos. 1-ZVAW, 1-ZVAL and B-Q26E). We thank Dr. W. Xie for helpful discussions.

Notes and references

[a]Department of Applied Physics, The Hong Kong Polytechnic University, Hong Kong, People's Republic of China.

[b]Shenzhen Research Institute, The Hong Kong Polytechnic University, Shenzhen, People's Republic of China.
[c]Department of Physics, The Chinese University of Hong Kong, Hong Kong, People's Republic of China.
[d]Key Lab of Advanced Transducers and Intelligent Control System of Ministry of Education, and College of Physics and Optoelectronics, Taiyuan University of Technology, Taiyuan, China.
‡Z. Y. B. and D. Y. L. contributed equally to this work.
*To whom correspondence may be addressed. Email: dylei@polyu.edu.hk or yuen.tsang@polyu.edu.hk.

1 V. Giannini, A. I. Fernández-Domínguez, S. C. Heck, and S. A. Maier, *Chem. Rev*., 2011, **111**, 3888.
2 A. Kinkhabwala, Z. F. Yu, S. H. Fan, Y. Avlasevich, K. Müllen and W. E. Moerner, *Nat. Photon*., 2009, **3**, 654.
3 K. Kneipp, H. Kneipp, I. Itzkan, R. R. Dasari, and M. S. Feld, *Chem. Rev*., 1999, **99**, 2957.
4 Y. Wang, B. Yan, L. Chen, *Chem. Rev.,* 2013, **113**, 1391.
5 S. Schlücker, *Angew. Chem. Int. Ed*., 2014, **53**, 4756.
6 A. O. Govorov, H. H. Richardson, *Nano Today*, 2007, 2, 30.
7 J.-W. Kim, E. I. Galanzha, E. V. Shashkov, H.-M. Moon, V. P. Zharov, *Nat. Photon*., 2009, **4**, 688.
8 P. Fang, S. Duan, X. Lin, J. R. Anema, J. Li, O. Buriez, Y. Ding, F. Fan, D. Wu, B. Ren, Z. L. Wang, C. Amatore and Z. Q. Tian, *Chem. Sci*., 2011, **2**, 531.
9 A. Marimuthu, J. W. Zhang, S. Linic, *Science,* 2013, 339, 1590.
10 Z. Y. Bao, X. Liu, J. Dai, Y. Wu, Y. H. Tsang, and D. Y. Lei, *Appl. Surf. Sci.*, 2014, **301**, 351.
11 H. Kim, K. M. Kosuda, R. P. Van Duyne, P. C. Stair, *Chem. Soc. Rev*., 2010,**39**, 4820.
12 J. Y. Chen, B. Wiley, J. McLellan, Y. J. Xiong, Z. Y. Li, Y. N. Xia, *Nano Lett*., 2005, **5**, 2058.
13 S. J. Guo, L. Wang, Y. Wang, Y. Fang, E. K. Wang, *J. Colloid Interface Sci*.,2007, **315**, 363.
14 S. Z. Zou, C. T. Williams, E. K. Y. Chen, M. J. Weaver, *J. Am. Chem. Soc*., 1998, **120**, 3811.
15 L. Guerrini, E. Lopez-Tobar, J. V. Garcia-Ramos, C. Domingo, S. Sanchez-Cortes, *Chem. Commun*., 2011,**47**, 3174.
16 K. Kim, K. L. Kim and K. S. Shin, *J. Phys. Chem. C*, 2011, **115**, 14844.
17 K. N. Heck, B. G. Janesko, G. E. Scuseria, N. J. Halas and M. S. Wong, *J. Am. Chem. Soc*., 2008, **130**, 16592.
18 W. Xie, C. Herrmann, K. Kompe, M. Haase and S. Schlücker, *J. Am. Chem. Soc*., 2011, **133**, 19302.
19 V. Joseph, C. Engelbrekt, J. Zhang, U. Gernert, J. Ulstrup and J. Kneipp, *Angew. Chem. Int. Ed*., 2012, **51**, 7592.
20 M. Cao, L. Zhou, X. Xu, S. Cheng, J. L. Yao and L. J. Fan, *J. Mater. Chem. A*, 2013, **1**, 8942.
21 Y. F. Huang, H. P. Zhu, G. K. Liu, D. Y. Wu, B. Ren and Z. Q. Tian, *J. Am. Chem. Soc.*, 2010, **132**, 9244.
22 D. Y. Wu, L. B. Zhao, X. M. Liu, R. Huang, Y. F. Huang, B. Ren, Z. Q. Tian, *Chem. Commun*., 2011, **47**, 2520.
23 E. M. van Schrojenstein Lantman, T. Deckert-Gaudig, A. J. G. Mank, V. Deckert and B. M. Weckhuysen, *Nat. Nanotechnol*., 2012, **7**, 583.
24 L. Li, T. Hutter, A. Finnermore, F. M. Huang, J. J. Baumberg, S. Elliot, U. Steiner and S. Mahajan, *Nano Lett.*, 2012, **12**,4242.
25 Z. Dai, X. Xiao, Y. Zhang, F. Ren, W. Wu, S. Zhang, J. Zhou, F. Mei and C. Jiang, *Nanotechnology,* 2012, **23**, 335701.
26 W. Xie, B. Walkenfort and S. Schlücker, *J. Am. Chem. Soc.*, 2013, **135**, 1657.
27 M. Sun, Z. Zhang, H. Zheng and H. Xu, *Sci. Rep.*, 2012, **2**, 647.
28 M. D. Xiao, R. B. Jiang, F. Wang, C. H. Fang, J. F. Wang, J. Yu, *J. Mater. Chem. A*, 2013, **1**, 5790.
29 S. Mukherjee, F. Libisch, N. Large, O. Neumann, L. V. Brown, J. Cheng, J. B. Lassiter, E. A. Carter, P. Nordlander and N. J. Halas, *Nano Lett*., 2013, **13**, 240.
30 W. Ni, X. Kou, Z. Yang and J. Wang, *ACS Nano,* 2008, **2**, 677.
31 D.-Y. Wu, X.-M. Liu, Y.-F. Huang, B. Ren, X. Xu, and Z.-Q. Tian, *J. Phys. Chem. C.* 2009, **113**, 18212.
32 Y.-F. Huang, H.-P. Zhu, G.-K. Liu, D.-Y. Wu, B. Ren, and Z.-T. Tian, *J. Am. Chem. Soc*., 2010, **132**, 9244.
33 R. Liu, J.-F. Liu, Z. -M. Zhang, L. -Q. Zhang, J. -F. Sun, M. -T. Sun, and G. -B. Jiang, *J. Phys. Chem. Lett*. 2014, **5**, 969.
34 Z. Y. Bao, J. Y. Dai, D. Y. Lei and Y. C. Wu, *J. Appl. Phys*., 2013, **114**, 124305.
35 Y. D. Zhao, X. Liu, D. Y. Lei and Y. Chai, *Nanoscale*, 2013, **6**, 1311.